applied sciences

MDPI

Article

Achievement of Accurate Robotic Arm-based Bike Frame Quality Check Using 3D Geometry Mathematical Model

Hsiung-Cheng Lin *, Bo-Ren Yu, Jen-Yu Wang, Jun-Ze Lai and Jia-Yang Wu

Department of Electronic Engineering, National Chin-Yi University of Technology, Taichung 41170, Taiwan; sdennil9999@gmail.com (B.-R.Y.); st831209@gmail.com (J.-Y.W.); hank081083@gmail.com (J.-Z.L.); sweet911105@gmail.com (J.-Y.W.)

* Correspondence: hclin@ncut.edu.tw

Received: 29 October 2019; Accepted: 6 December 2019; Published: 8 December 2019

Abstract: Currently, the bike frame quality check (QC) mostly relies on human operation in industry. However, some drawbacks such as it being time-consuming, having low accuracy and involving non-computerized processes are still unavoidable. Apart from these problems, measured data are difficult to systematically analyze for tracking sources of product defects in the production process. For this reason, this paper aims to develop a 3D geometry mathematical model suitable for bicycle frames QC using robotic arm-based measurement. Unlike the traditional way to find coefficients of a space sphere, the proposed model requires only three check point coordinates to achieve the sphere axis coordinate and its radius. In the practical work, the contact sensor combined with the robotic arm is used to realize the compliance items measurement in shaft length, internal diameter, verticality, parallelism, etc. The proposed model is validated based on both mathematic verification and actual bike frame check.

Keywords: quality check; bike frame; mathematical model; graphical user interface

1. Introduction

In recent years, bike riding has become a popular leisure sport around the world. For this reason, analysts forecast that the global high-end bicycle market will grow with a compound annual growth rate (CAGR) of 4.82% during the period 2017–2021 according to the report from Research and Markets Ltd. It is known that high-end bikes demand a high quality of bike frame [1–7]. Unfortunately, frame QC still relies on the Vernier caliper, the plug gauge, the cylindrical gauge, and the thread gauge, etc. It normally takes a long time to complete the process. Consequently, the automation measurement process for the QC of the bike frame is essential in industry [8–12].

The coordinate-measuring-machine (CMM) is now being widely applied as part of workpiece inspection in the production line [13–17]. It can be used to measure the geometry of physical objects by sensing the discrete points on the object surface with a probe, including mechanical, optical, laser, and white light. Basically, it has two major advantages: (1) high precision up to 0.001 mm and (2) high reliability in both hardware and software. However, the CMM inspection planning session has been a challenging issue because of its time-consuming nature using traditional methods, e.g., expert experiences and technical documents data mining. Additionally, it may suffer from some following disadvantages: (1) Its operation speed is limited. (2) It is sensitive to the environment temperature and humidity. (3) It is not applicable to irregular shape object measurements. (4) It has a high cost. Obviously, CMM is not suitable for the bike frame measurement due to the restriction of the operation range. Alternatively, robotic arms are typically used for multiple industrial applications such as

material handling, welding, thermal spraying, assembly, palletizing, drilling, and painting, etc. [18–21]. For instance, a platform based on a robotic arm using three degrees of freedom (DoF) principle was proposed to estimate the calibration parameters of microelectromechanical systems (MEMS) [22]. It can be placed indifferent positions for collecting a dataset of points evenly distributed. This case implies that the measurement technique using robotic arms may provide a good solution for the bike frame QC process.

2. System Description

2.1. System Structure

The proposed system structure of bike frame quality check is shown in Figure 1a, consisting of subsystems such as robotic arm, graphical user interface (GUI), programmable logic controller (PLC), contact sensor, mathematical model, database, and workbench. Each subsystem is responsible to carry out a specific task, described as follows. (1) Robotic arm can carry the contact sensor and move it to the check points. Therefore, the coordinates of check points can be found based on the robotic arm coordinate system. (2) The contact sensor can feedback a digital signal to the robotic arm immediately once it touches the surface of the check points. (3) PLC is to control the rotating disk to rotate the bike frame 90° for the robotic arm to reach every check point. (4) Graphical user interface (GUI) provides a friendly user interface for users to input data and display a real-time measurement outcome. (5) Mathematical model presents a geometry algorithm that can effectively integrate the sphere formula with the inner product of normal vector to find four parameters in the sphere formula using only three measured points. Accordingly, the center coordinate of check point and its diameter can be calculated accurately and simply. (6) A database using MySQL is used to store the measured data and export measurement data report. (7) The workbench shown in Figure 1b is designed to sustain all hardware devices. It contains: (1) a fixing frame, (2) A rotating disk, (3) a work platform, and (4) a sensor pedestal. Moreover, the XAML and C# package are used to build up the system software such as the robotic arm simulation object, the window object, the control object, and the 3D-geometry mathematical model. Through Transmission Control Protocol (TCP) and Internet Protocol (IP) (TCP/IP), the contact sensor and robotic arm can communicate with each other between different objects.

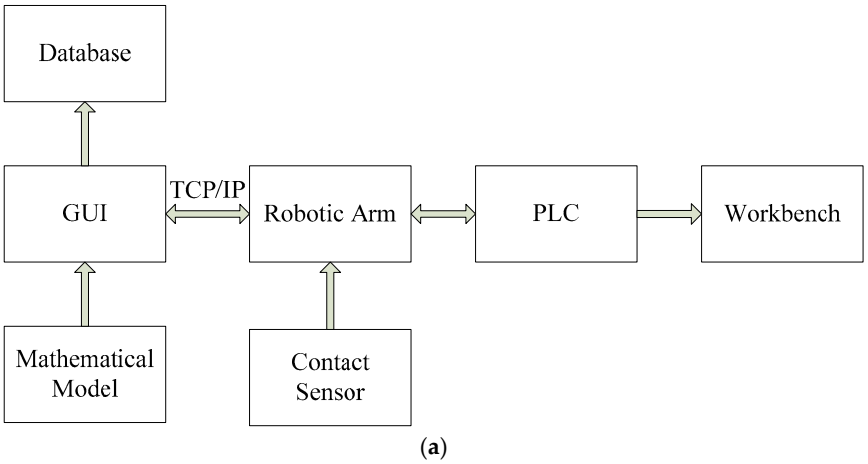

(**a**)

Figure 1. *Cont.*

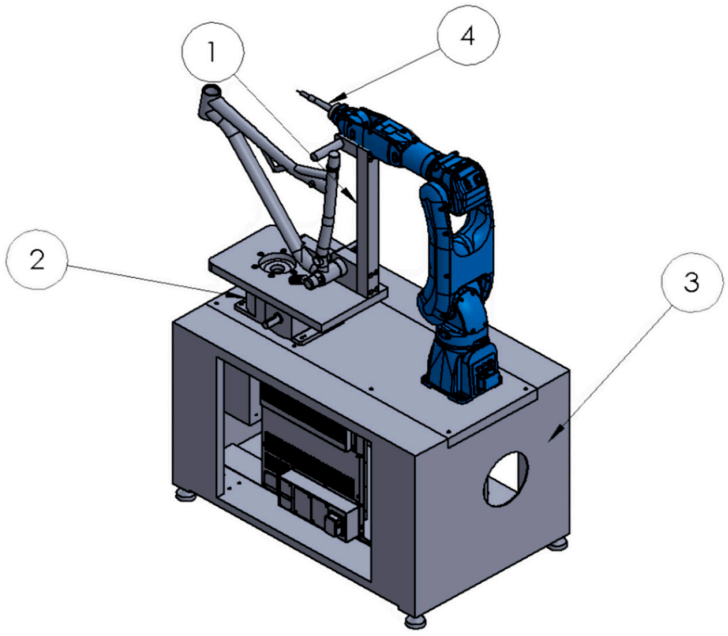

(**b**)

Figure 1. System structure: (**a**) system block; (**b**) profile of workbench.

In this study, we mainly focused on the development of mathematical model required for the bike frame quality check using a robotic arm. Based on the proposed mathematical model, the robotic arm is combined with the contact sensor to implement the bike frame quality check in shaft length, internal diameter, verticality, and parallelism, etc. The major devices used in the proposed system are listed as follows:

(1) Robotic arm: YASKAWA-GP7
(2) Contact sensor: Compact module changing touch-trigger probe (Renishaw TP20)
(3) PLC: DELTA DVP –PM1000M
(4) Database: MySQL

2.2. Introduction of Bike Frame

Generally, the bike frame consists of: (1) a B.B rotating shaft, (2) a S/T rotating shaft, (3) a S/T groove, (4) a T/T rotating shaft, (5) a shock absorber, (6) and H/T, where they are required for quality check, as shown in Figure 2.

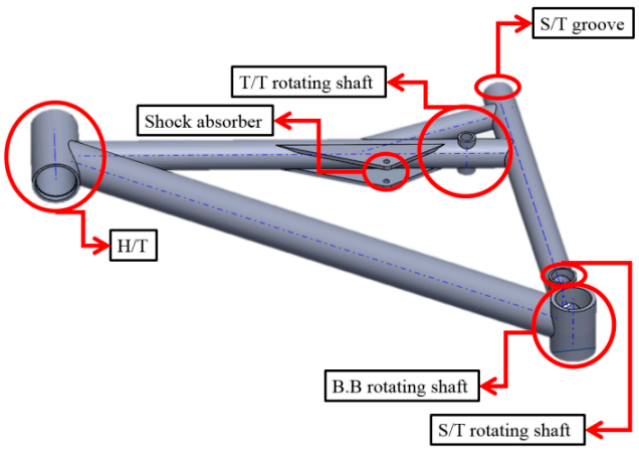

Figure 2. Profile of a bike frame.

3. Mathematical Model

The check items of bike frame for quality evaluation mainly include the shaft length, internal diameter, verticality, and parallelism located in different shafts. The proposed mathematical model provides the solutions for checked point coordinate calculation. It is described as follows.

3.1. Generation of Bike Frame Center Plane

Initially, the center plane of a bike frame should be generated from the B.B rotating shaft, as shown in Figure 3, which is used as the base of the coordinate system. The coordinate of the center point $aa3(aa3_x, aa3_y, aa3_z)$, as shown in Figure 3, can be determined from $aa1(aa1_x, aa1_y, aa1_z)$ and $aa2(aa2_x, aa2_y, aa2_z)$ as:

$$aa3_x = \frac{aa1_x + aa2_x}{2} \qquad aa3_y = \frac{aa1_y + aa2_y}{2} \qquad aa3_z = \frac{aa1_z + aa2_z}{2}$$

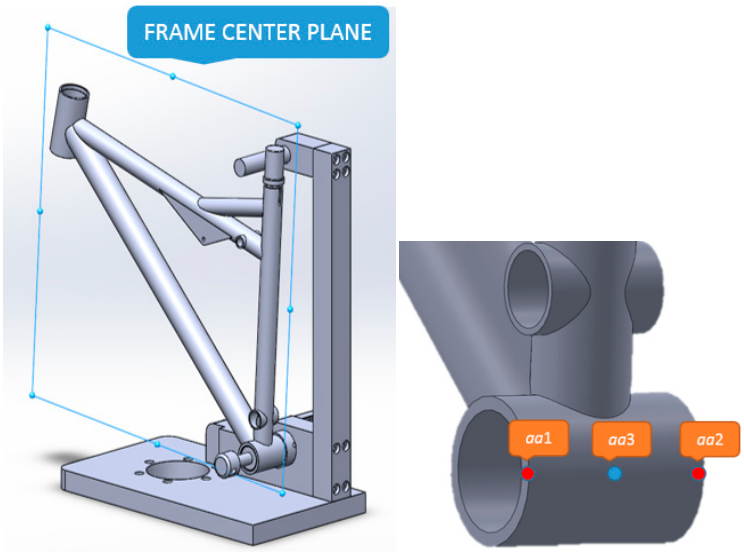

Figure 3. The center plane (**left**) and point (**right**) of bike frame.

3.2. Center Plane Offset

The center plane offset is used to check if there is a shift at the center plane. For this purpose, the y-axis $aa3_y$ taken from the center point $aa3(aa3_x, aa3_y, aa3_z)$ is regarded as the center standard plane.

In Figure 4, two check points, i.e., $cc1$ and $cc22$, coordinates at the S/T rotating shaft are expressed as:

$$cc1(cc1_x, cc1_y, cc1_z) \qquad cc22(cc22_x, cc22_y, cc22_z)$$

cc is defined as the center point between $cc1$ and $cc22$ as:

$$cc\left(\frac{cc1_x + cc22_x}{2}, \frac{cc1_y + cc22_y}{2}, \frac{cc1_z + cc22_z}{2}\right)$$

$w1$ shown in Equation (1) is defined as the center plane offset at the S/T rotating shaft, and it is the distance between the y axis coordinate of the cc point and the center plane.

$$w1 = \left|\frac{cc1_y + cc22_y}{2} - aa3_y\right| \tag{1}$$

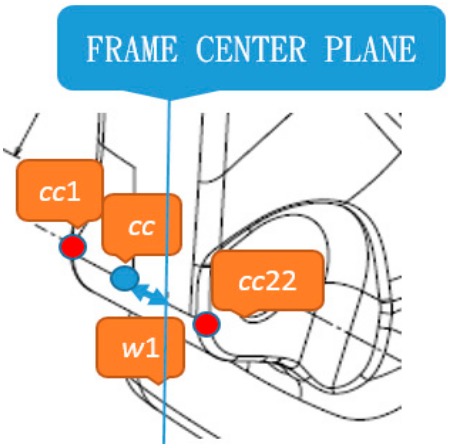

Figure 4. Center plane offset.

3.2.1. H/T Rotating Shaft Length

The H/T rotating shaft length can be determined by taking eight check points, as shown in Figure 5.

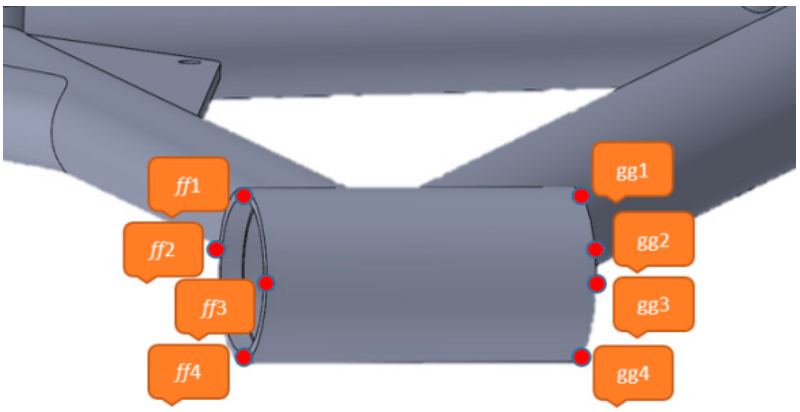

Figure 5. Check points of H/T rotating shaft length.

The coordinates of the eight check points are shown as follows:

$ff1(ff1_x, ff1_y, ff1_z)$ $ff2(ff2_x, ff2_y, ff2_z)$ $ff3(ff3_x, ff3_y, ff3_z)$ $ff4(ff4_x, ff4_y, ff4_z)$
$gg1(gg1_x, gg1_y, gg1_z)$ $gg2(gg2_x, gg2_y, gg2_z)$ $gg3(gg3_x, gg3_y, gg3_z)$ $gg4(gg4_x, gg4_y, gg4_z)$

The length $\overline{ff1gg1}$ between two check points ($ff1$ and $gg1$) is:

$$\overline{ff1gg1} = \sqrt{(gg1_x - ff1_x)^2 + \left(gg1_y - ff1_y\right)^2 + (gg1_z - ff1_z)^2} \quad (2)$$

Similarly, the lengths $\overline{ff2gg2}$, $\overline{ff3gg3}$, and $\overline{ff4gg4}$ can be formulated according to Equation (2), where the number one changes to numbers two to four, respectively.

Average length (L) between two check points ($ff2$ and $gg2$) is:

$$\mathrm{L} = \frac{\overline{ff1gg1} + \overline{ff2gg2} + \overline{ff3gg3} + \overline{ff4gg4}}{4} \quad (3)$$

3.2.2. T/T Rotating Shaft Internal Diameter

The three check points at the T/T rotating shaft can be used to calculate the internal diameter, as shown in Figure 6.

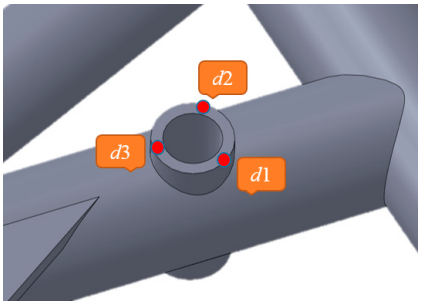

Figure 6. The three check points at the T/T rotating shaft.

The coordinates of the three check points are expressed as:

$$d1(d1_x, d1_y, d1_z) \qquad d2(d2_x, d2_y, d2_z) \qquad d3(d3_x, d3_y, d3_z)$$

The vectors $\overrightarrow{d_3d_1}$ and $\overrightarrow{d_3d_2}$ are:

$$\overrightarrow{d_3d_1} = \left((d1_x - d3_x), \left(d1_y - d3_y\right), (d1_z - d3_z)\right) \tag{4}$$

$$\overrightarrow{d_3d_2} = \left((d2_x - d3_x), \left(d2_y - d3_y\right), (d2_z - d3_z)\right) \tag{5}$$

The use cross product for the vectors $\overrightarrow{d_3d_1}$ and $\overrightarrow{d_3d_2}$, and their normal vector $\vec{n}$ can be obtained as:

$$\vec{n} = \overrightarrow{d_3d_2} \times \overrightarrow{d_3d_1} = \left(n_x, n_y, n_z\right) \tag{6}$$

where

$$n_x = \begin{vmatrix} \left(d2_y - d3_y\right) & (d2_z - d3_z) \\ (d1_z - d3_z) & \left(d1_y - d3_y\right) \end{vmatrix}$$

$$n_y = -\begin{vmatrix} (d2_x - d3_x) & (d2_z - d3_z) \\ (d1_x - d3_x) & (d1_z - d3_z) \end{vmatrix}$$

$$n_z = \begin{vmatrix} (d2_x - d3_x) & \left(d2_y - d3_y\right) \\ (d1_x - d3_x) & \left(d1_y - d3_y\right) \end{vmatrix}$$

The spherical general shown in Equation (7) is used to find the axis point coordinate and axial bore radius in Figure 6:

$$x^2 + y^2 + z^2 + dx + ey + fz + g = 0 \tag{7}$$

where the spherical axis point coordinate ($d4$) in Figure 6 is $\left(\frac{-d}{2}, \frac{-e}{2}, \frac{-f}{2}\right)$, and d, e, f, and g are real numbers.

The vector $\overrightarrow{d_4d_3}$ can be obtained as:

$$\overrightarrow{d_4d_3} = \left((d3_x) - \left(\frac{-d}{2}\right), \left(d3_y\right) - \left(\frac{-e}{2}\right), (d3_z) - \left(\frac{-f}{2}\right)\right) \tag{8}$$

The vectors $\overrightarrow{d_4d_3}$ and $\vec{n}$ are perpendicular to each other so that their inner product is zero.

$$\overrightarrow{d_4d_3} \cdot \vec{n} = 0 \tag{9}$$

Following this, we substitute the coordinates of three check points $d1(d1_x, d1_y, d1_z)$, $d2(d2_x, d2_y, d2_z)$, $d3(d3_x, d3_y, d3_z)$ into Equation (7) to form Equations (10)–(12). Additionally, Equation (13) is obtained based on Equation (9).

$$(d1_x)^2 + \left(d1_y\right)^2 + (d1_z)^2 + d(d1_x) + e\left(d1_y\right) + f(d1_z) + g = 0 \tag{10}$$

$$(d2_x)^2 + \left(d2_y\right)^2 + (d2_z)^2 + d(d2_x) + e\left(d2_y\right) + f(d2_z) + g = 0 \tag{11}$$

$$(d3_x)^2 + \left(d3_y\right)^2 + (d3_z)^2 + d(d3_x) + e\left(d3_y\right) + f(d3_z) + g = 0 \tag{12}$$

$$\begin{vmatrix} \left(d2_y - d3_y\right) & (d2_z - d3_z) \\ (d1_z - d3_z) & \left(d1_y - d3_y\right) \end{vmatrix} \left|\left((d3_x) - \left(\tfrac{-d}{2}\right)\right) - \begin{vmatrix} (d2_x - d3_x) & (d2_z - d3_z) \\ (d1_x - d3_x) & (d1_z - d3_z) \end{vmatrix} \left|\left(\left(d3_y\right) - \left(\tfrac{-e}{2}\right)\right)\right.\right. + \begin{vmatrix} (d2_x - d3_x) & \left(d2_y - d3_y\right) \\ (d1_x - d3_x) & \left(d1_y - d3_y\right) \end{vmatrix} \left|\left((d3_z) - \left(\frac{-f}{2}\right)\right) = 0\right. \tag{13}$$

The parameters values (d, e, f, g) can be thus be found by solving the simultaneous equations from Equations (10)–(13).

Consequently, $d_4\left(\frac{-d}{2}, \frac{-e}{2}, \frac{-f}{2}\right)$ can be obtained, and the axial bore radius of T/T rotating shaft can be calculated as:

$$\overline{d_4 d_1} = \overline{d_4 d_2} = \overline{d_4 d_3} = \frac{1}{2}\sqrt{d^2 + e^2 + f^2 - 4g} \tag{14}$$

3.2.3. Parallelism

In Figure 7, the parallelism angle between B.B. and T/T rotating shafts can be calculated as follows:

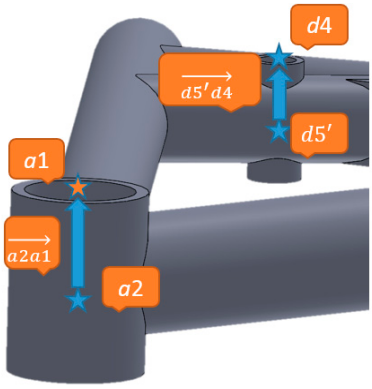

Figure 7. The parallelism between B.B. and T/T rotating shafts.

$$\overrightarrow{a2a1} = \left((a1_x - a2_x), \left(a1_y - (-333.5)\right), (a1_z - a2_z)\right) \tag{15}$$

$$\overrightarrow{d5'd4} = \left(0, \left(d4_y - \frac{\left(d1_y + d11_y\right)}{2}\right), 0\right) \tag{16}$$

Using the inner product formula, the parallelism angel θ between $\overrightarrow{a2a1}$ and $\overrightarrow{d5'd4}$ can be calculated as:

$$\cos\theta = \frac{\overrightarrow{d5'd4} \cdot \overrightarrow{a2a1}}{\left|\overrightarrow{d5'd4}\right| \left|\overrightarrow{a2a1}\right|} \tag{17}$$

3.2.4. Verticality

In Figure 8, the verticality angel between B.B. and H/T rotating shafts can be calculated as follows.

$$\overrightarrow{a2g4} = \Big((g4_x - a2_x), \big(g4_y - (-333.5)\big), (g4_z - a2_z)\Big) \tag{18}$$

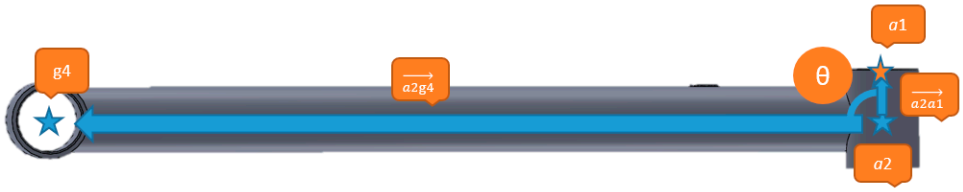

Figure 8. The verticality angel between the B.B. rotating shaft and the H/T rotating shaft.

Use the inner product formula, the verticality angel θ between $\overrightarrow{a2a1}$ and $\overrightarrow{a2g4}$ can be calculated as:

$$\cos\theta = \frac{\overrightarrow{a2a1} \cdot \overrightarrow{a2g4}}{\left|\overrightarrow{a2a1}\right| \left|\overrightarrow{a2g4}\right|} \tag{19}$$

4. Model Verification Using the Real Data

The proposed mathematical model is verified using the real data taken from the SOLIDWORKS drawing of the bike frame.

4.1. The Center Plane

From Figure 3, the two check points are:

$$aa1(139.59, -297, 109.14) \qquad aa2(139.59, -370, 108.85)$$

The center point of B.B rotating shaft is $aa3(aa3_x, aa3_y, aa3_z)$, where:

$$aa3_x = \frac{139.59 + 139.59}{2} = 139.59$$
$$aa3_y = \frac{-297 + (-370)}{2} = -333.5$$
$$aa3_z = \frac{109.14 + 108.85}{2} = 108.995$$
$$\therefore \quad aa3(139.59, -333.5, 108.995)$$

Accordingly, the center plane is located at $aa3_y = -333.5$mm.

4.2. Bike Center Plane Offset

From Figure 4, it is known that:

$$cc1(107.23, -373.75, 138.38) \qquad cc2(107.23, -327.25, 138.38)$$

The cc is located at the center point between $cc1$ and $cc2$.
Therefore,

$$cc(107.23, -350.5, 138.38)$$
$$w1 = \left|-350.5 - (-333.5)\right| = 17\text{mm}$$

As above, it is confirmed that the theoretical value matches the computational result.

4.3. The H/T Rotating ShaftLength

In Figure 5, the coordinates of eight check points are shown as follows.

$ff1(625.05, 123.58, 600.41)$ $ff2(598.67, 150.63, 594.12)$ $ff3(650.93, 151.37, 606.57)$
$ff4(624.70, 177.33, 600.32)$ $gg1(651.01, 123.77, 493.51)$ $gg2(623.60, 150.68, 486.98)$
$gg3(676.13, 149.86, 499.50)$ $gg4(649.70, 177.24, 493.20)$

Accordingly,

$$\overline{ff1gg1} = \sqrt{(651.01-625.05)^2+(123.77-123.58)^2+(493.51-600.41)^2} \cong 110\text{mm}$$
$$\overline{ff2gg2} = \sqrt{(623.60-598.67)^2+(150.68-150.63)^2+(486.98-594.12)^2} \cong 110\text{mm}$$
$$\overline{ff3gg3} = \sqrt{(676.13-650.93)^2+(149.86-151.37)^2+(499.50-606.57)^2} \cong 110\text{mm}$$
$$\overline{ff4gg4} = \sqrt{(649.70-624.70)^2+(177.24-177.33)^2+(493.20-600.32)^2} \cong 110\text{mm}$$

The average length (L) is obtained as:

$$\text{L} = \frac{\overline{ff1gg1+ff2gg2+ff3gg3+ff4gg4}}{4} \cong 110\text{mm}$$

As above, the calculated value is confirmed equal to the theoretical value.

4.4. T/T Rotating Shaft Internal Diameter

In Figure 6, the coordinates of three check points ($d1$, $d2$, $d3$) are shown as follows:

$d1 = (55.39, 24, 353.63)$ $d2 = (55.85, 24, 366.87)$ $d3 = (66.64, 24, 359.98)$

Therefore,

$$\begin{aligned} \overrightarrow{d3d1} &= (-11.25, 0, -6.35) \\ \overrightarrow{d3d2} &= (-10.79, 0, 6.89) \\ \vec{n} = \overrightarrow{d3d2} \times \overrightarrow{d3d1} &= \left(n_x, n_y, n_z\right) \end{aligned} \tag{20}$$

where;

$$n_x = \begin{vmatrix} 0 & 6.89 \\ 0 & -6.35 \end{vmatrix} = 0$$
$$n_y = \begin{vmatrix} -10.79 & 6.89 \\ -11.25 & -6.35 \end{vmatrix} = -146.029$$
$$n_z = \begin{vmatrix} -10.79 & 0 \\ -11.25 & 0 \end{vmatrix} = 0$$
$$\vec{n} = (0, -146.029, 0)$$

According to Equation (7), the axis point coordinate is $d4\left(\frac{-d}{2}, \frac{-e}{2}, \frac{-f}{2}\right)$.

Therefore,

$$\overrightarrow{d4d3} = \left(66.64 - \left(\frac{-d}{2}\right), 24 - \left(\frac{-e}{2}\right), 359.98 - \left(\frac{-f}{2}\right)\right) \tag{21}$$

$\overrightarrow{d4d3}$ and $\vec{n}$ are perpendicular to each other so that:

$$\overrightarrow{d4d3} \cdot \vec{n} = 0$$

$\Rightarrow$

$$0 \cdot \left(66.64 - \left(\frac{-d}{2}\right)\right) - 146.029 \cdot \left(24 - \left(\frac{-e}{2}\right)\right) + 0 \cdot \left(359.98 - \left(\frac{-f}{2}\right)\right) = 0 \tag{22}$$

$$e = -48 \tag{23}$$

Substitute the coordinates of $d1$, $d2$ and $d3$ into Equation (10), as follows.

$$(55.39)^2 + (24)^2 + (353.63)^2 + d(55.39) + e(24) + f(353.63) + g = 0 \tag{24}$$

$$(55.85)^2 + (24)^2 + (366.87)^2 + d(55.85) + e(24) + f(366.87) + g = 0 \tag{25}$$

$$(66.64)^2 + (24)^2 + (359.98)^2 + d(66.64) + e(24) + f(359.98) + g = 0 \tag{26}$$

$\Rightarrow$

$d = -118.27901$ $f = -720.25544$ $g = 133709.17771$

As above, it can be obtained:

$$d4\left(\frac{-d}{2}, \frac{-e}{2}, \frac{-f}{2}\right) = d4(59.1395, 24, 360.12772)$$

The radius between the axis and check point is:

$$\overline{d4d1} = \overline{d4d2} = \overline{d4d3} = \frac{1}{2}\sqrt{d^2 + e^2 + f^2 - 4g} \cong \frac{15}{2}(\text{mm}) \tag{27}$$

Accordingly, the internal diameter of T/T rotating shaft is:

$$= \sqrt{d^2 + e^2 + f^2 - 4g} \cong 15\text{mm}$$

As above, the calculated value is confirmed equal to the theoretical value.

4.5. Parallelism Between T/T and B.B Rotating Shafts Axes

In Figure 8, the coordinates of two check points ($d1$, $d11$) are:

$d1(55.39, 24, 353.63)$ $d11(55.39, -24, 353.63)$

The coordinate of middle point $d5$ located between $d1$ and $d2$ is:

$$d5(55.39, 0, 353.63)$$

The X-axis and Y-axis coordinates of axis point $d4$ at the T/T rotating shaft are transferred to d5 to form $d5'$. Therefore, the vector formed by $d4$ and $d5'$ is $\overrightarrow{d5'd4}$.

$$\begin{aligned} d5' &= (59.1395, 0, 360.12772) \\ \overrightarrow{d5'd4} &= (0, 24, 0) \end{aligned} \tag{28}$$

In Figure 7,

$a1(94.98, 48, 723.32)$ $a2(94.98, -333.5, 723.32)$

$\overrightarrow{a2a1}$ at the B.B rotating shaft is:

$$\overrightarrow{a2a1} = (0, 48 - (-333.5), 0) = (0, 381.5, 0) \tag{29}$$

The parallelism angel (θ) between $\overrightarrow{a2a1}$ and $\overrightarrow{d5'd4}$ can be calculated as:

$$\cos\theta = \frac{\overrightarrow{d5'd4} \cdot \overrightarrow{a2a1}}{\left|\overrightarrow{d5'd4}\right|\left|\overrightarrow{a2a1}\right|} = \frac{(0, 24, 0) \cdot (0, 381.5, 0)}{\left|(0, 24, 0)\right| \cdot \left|(0, 381.5, 0)\right|} = \frac{9156}{9156} = 1 \tag{30}$$

$$\therefore \theta = 0^{\circ}$$

As above, the T/T and B.B rotating shafts axes are confirmed parallel.

4.6. Verticality Between H/T and B.B Rotating Shafts Axes

The vector $\overrightarrow{a2g4}$ from the B.B rotating shaft to H/T axis point (g4) is:

$$\overrightarrow{a2g4} = (559.7486, -5, -154.8109)$$

where $a2(94.98, -333.5, 723.32)$ and $g4(654.7286, -338.5, 568.5091)$.

The verticality angel (θ) between $\overrightarrow{a2a1}$ and $\overrightarrow{a2g4}$ can be calculated as:

$$\cos\theta = \frac{\overrightarrow{a2a1} \cdot \overrightarrow{a2g4}}{\left|\overrightarrow{a2a1}\right| \left|\overrightarrow{a2g4}\right|} = \frac{(0, 381.5, 0) \cdot (559.7486, -5, -154.8109)}{\left|(0, 381.5, 0)\right| \cdot \left|(559.7486, -5, -154.8109)\right|} = \frac{-1907.5}{381.5 \times 580.7839} = -0.0086 \cong 0 \quad (31)$$

$$\therefore \theta = 90^{\circ}$$

As above, the H/T and B.B rotating shafts axes are confirmed vertical.

5. Practical Verification

The process of real bike frame quality check is carried out based on the proposed 3D geometry mathematical model. The real system profile is shown in Figure 9.

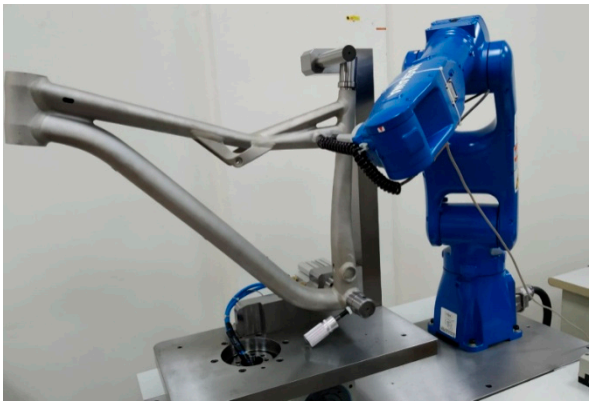

Figure 9. Profile of real measurement system.

5.1. Results with GUI

The quality check results are displayed online using GUI, as shown from Figures 10–15.

5.1.1. Bike Frame Plane

The GUI of the bike frame plane is shown in Figure 10. The performance result is –333.5 mm and that matches the theoretical value.

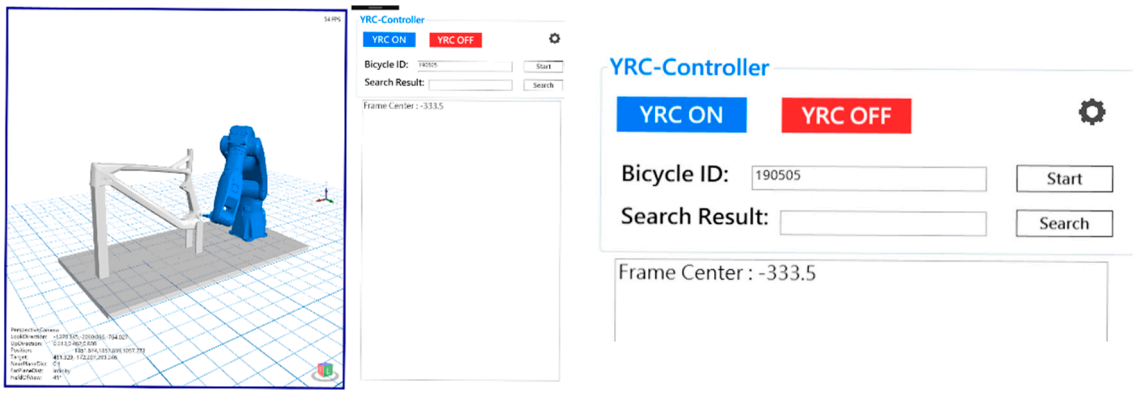

Figure 10. Graphical user interface (GUI) of the bike frame plane: (**a**) synchronous action; (**b**) GUI.

5.1.2. Bike Center Plane Offset

The GUI of bike center plane offset is shown in Figure 11. The performance result is 17 mm and that matches the theoretical value.

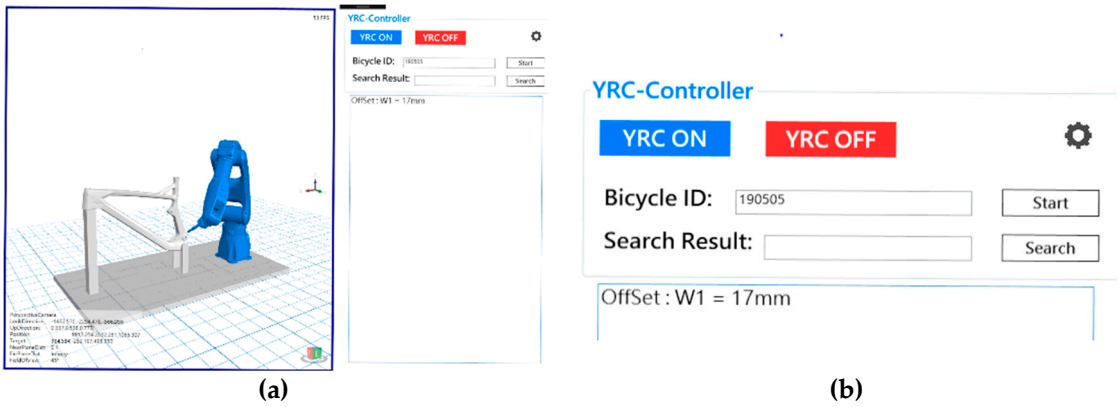

Figure 11. GUI of the bike center plane offset: (**a**) synchronous action; (**b**) GUI result.

5.1.3. H/T Rotating Shaft Length

The GUI of H/T rotating shaft length is shown in Figure 12. The performance result is 110 mm and that matches the theoretical value.

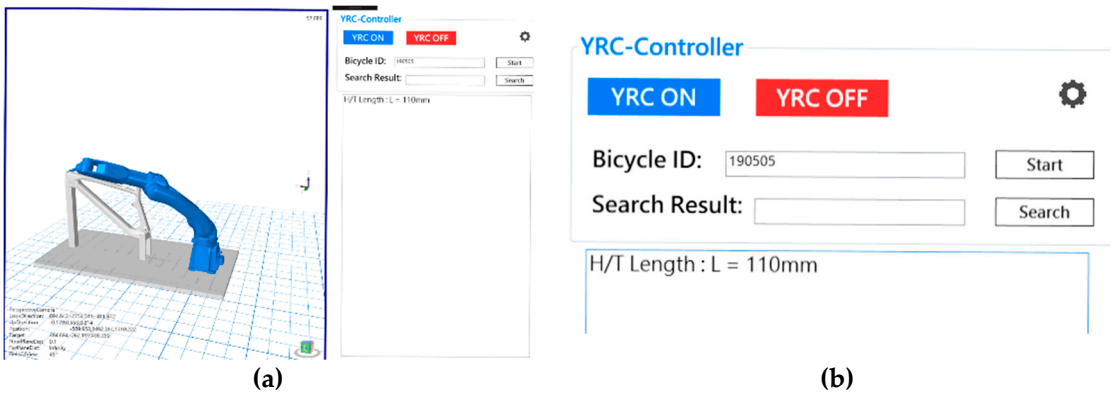

Figure 12. GUI of the H/T rotating shaft length: (**a**) synchronous action; (**b**) GUI result.

5.1.4. T/T Rotating Shaft Internal Diameter

The GUI of T/T rotating shaft internal diameter is shown in Figure 13. The performance result is 15 mm and that matches the theoretical value.

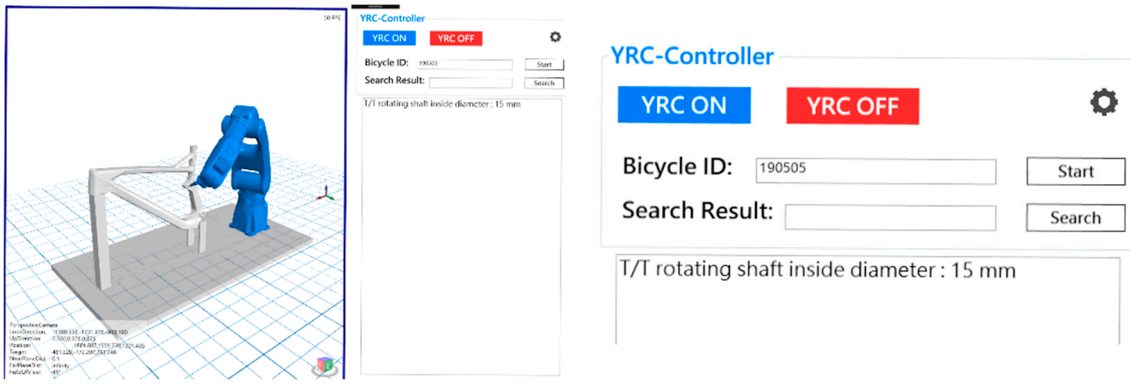

Figure 13. GUI of the T/T rotating shaft internal diameter: (**a**) synchronous action; (**b**) GUI result.

5.1.5. Parallelism

The parallelism between T/T and B.B rotating shafts axes using GUI is shown in Figure 14. The performance result is $\theta = 0^{\circ}$ that matches the theoretical value.

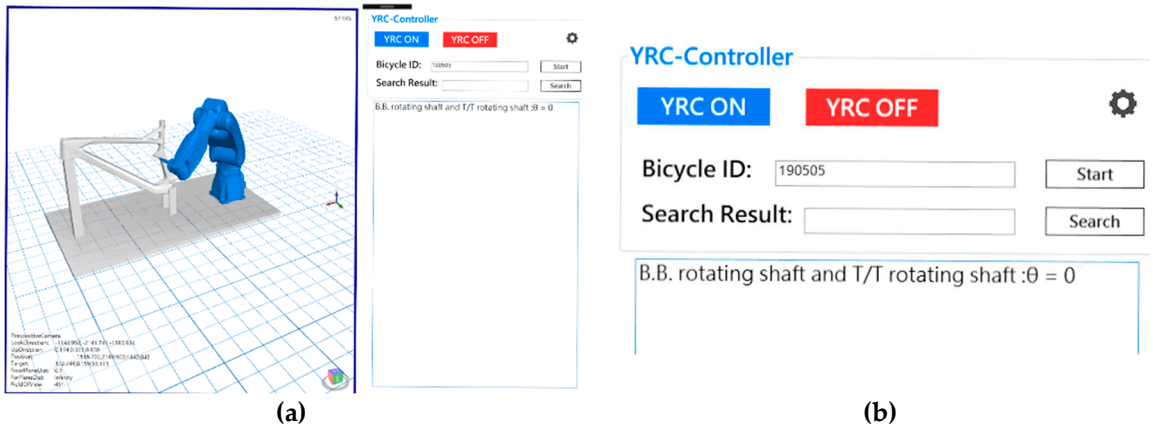

Figure 14. GUI of parallelism: (**a**) synchronous action; (**b**) GUI result.

5.1.6. Verticality

The verticality between H/T and B.B rotating shafts axes using GUI is shown in Figure 15. The performance result is $\theta = 90^{\circ}$ that matches the theoretical value.

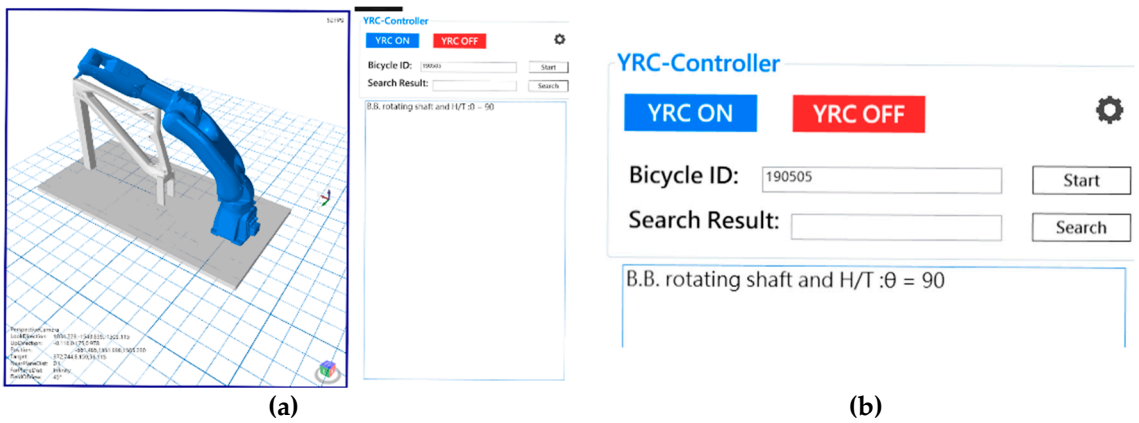

Figure 15. GUI of verticality: (**a**) synchronous action; (**b**) GUI result.

5.2. Practical Results

The measurement results from 10-times average values using the real bike frame are concluded in Table 1. Based on the same bike frame, the error between the proposed model and the Vernier caliper is below 0.05 mm, and the repeatability is at the range of 0.1 mm. This verifies that the proposed model presents both robust and stable performance. Nevertheless, the measured data reveals that the tested frame has some defects occurred in the center plane offset, parallelism and verticality.

Table 1. Measured values using the proposed model.

Check Point / Check Item	T/T Rotating Shaft	H/T Rotating Shaft
Center plane offset	−2.71 mm	Not applicable
Parallelism	8.2°	Not applicable
Verticality	Not applicable	114.65°
Internal diameter	14.86 mm	Not applicable
Length	Not applicable	109.89 mm

To clarify the uncertainty of the measurement, the estimated standard deviation for a series of n measurements is expressed mathematically as:

$$s = \sqrt{\frac{\sum_{i=1}^{n} (x_i - \overline{x})^2}{n-1}} \tag{32}$$

where x_i is the result of the ith measurement and $\overline{x}$ is the arithmetic mean of the n measurement results.

When a set of several repeated readings has been taken, the mean, $\overline{x}$, and estimated standard deviation, s, can be calculated. The measurement uncertainty, u, of the mean is therefore defined as:

$$u = \frac{s}{\sqrt{n}} \tag{33}$$

where n is the number of measurements in the set.

The estimated standard deviation and measurement uncertainty based on 10 measurements for S/T rotating shaft, T/T rotating shaft, and H/T rotating shaft is shown in Tables 2–4, respectively. From the statistics, it is obvious that both standard deviation (s) and measurement uncertainty (u) for all shaft measurements present a very low value no more than 0.018. Thus, accuracy and robustness of the proposed model is thus confirmed.

Table 2. Standard deviation (s) and measurement uncertainty (u) at S/T rotating shaft.

Estimated Topic / Check Item	Standard Deviation (s)	Measurement Uncertainty (u)
Center Plane Offset	0.007	0.002
Internal Diameter	0.009	0.003
Length	0.006	0.002
Parallelism	0.010	0.003

Table 3. Standard deviation (s) and measurement uncertainty (u) at T/T rotating shaft.

Estimated Topic / Check Item	Standard Deviation (s)	Measurement Uncertainty (u)
Center Plane Offset	0.005	0.002
Internal Diameter	0.018	0.006
Length	0.007	0.002
Parallelism	0.011	0.003

Table 4. Standard deviation (s) and measurement uncertainty (u) at H/T rotating shaft.

Estimated Topic / Check Item	Standard Deviation (s)	Measurement Uncertainty (u)
Internal Diameter	0.007	0.002
Length	0.005	0.002
Verticality	0	0

6. Conclusions

Traditional methods for the QC of bike frame products usually use general jigs or Vernier calipers. However, this kind of measurement process may take tens of minutes to complete. Another disadvantage is that it is difficult to analyze the measured data due to lack of computerization. For these reasons, the proposed 3D geometry mathematical model has successfully developed an accurate bike frame measurement based on a robotic arm with a contact sensor. In this study, the proposed model requires only three simultaneous equations to find the axis coordinate and its radius instead of four equations in a space sphere. It verifies that the measured data obtained from the model performance is consistent with the SOLIDWORKS drawing, including H/T rotating shaft length, T/T rotating shaft internal diameter, parallelism, and verticality, etc. Accordingly, it is applicable for industrial QC applications in a variety of bike frames. Other than these advantages, the stylus probe used in this proposed model presents both simple and accurate performance. However, successful measurement depends on the activity range of robotic arm that the certain features of bike frames should be reached by the stylus probe. In the future work, the optical sensors used in CMM may provide an alternative solution, although more complex signal processing algorithm should be addressed.

Author Contributions: All authors conceived the study. H.-C.L. led the project and wrote this article. B.-R.Y. built the mathematical model. J.-Y.W. (Jen-Yu Wang) designed the system software. J.-Z.L. wrote the robotic-arm control program. J.-Y.W. (Jia-Yang Wu) designed the system mechanism.

Funding: This work was supported by the Ministry of Science and Technology, Taiwan (grant number MOST 108-2637-E-167-001).

Conflicts of Interest: The authors declare no conflict of interest.

References

1. Cicero, S.; Lacalle, R.; Cicero, R.; Fernández, D.; Méndez, D. Analysis of the cracking causes in an aluminium alloy bike frame. *Eng. Fail. Anal.* **2011**, *18*, 36–46. [CrossRef]
2. Collotta, M.; Solazzi, L.; Pandini, S.; Tomasoni, G. New design concept of a downhill mountain bike frame made of a natural composite material. In *The Institution of Mechanical Engineers, Part P: Journal of Sports Engineering and Technology, Proceedings of the Institution of Mechanical Engineers*; The Institution of Mechanical Engineers: London, UK, 2018; pp. 50–56.
3. Priadythama, I.; Suhardi, B.; Adiasa, I. Further study on a short wheel base recumbent bike frame using simulated finite element analysis. In Proceedings of the 2016 2nd International Conference of Industrial, Mechanical, Electrical, and Chemical Engineering, Yogyakarta, Indonesia, 6–7 October 2016. [CrossRef]
4. Chang, C.T.; Huang, Y.C.; Chen, S.Y. Design optimization and automation of metal and composite bike frame. In Proceedings of the International SAMPE Technical Conference, Baltimore, MD, USA, 18–21 May 2015; pp. 1–18.
5. Collins, P.K.; Leen, R.; Gibson, I. Industry case study: Rapid prototype of mountain bike frame section. *Virtual. Phys. Prototyp.* **2016**, *11*, 295–303. [CrossRef]
6. Vdovin, D.; Chichekin, I.; Ryakhovsky, O. Quad bike frame dynamic load evaluation using full vehicle simulation model. *IOP Conf. Ser. Mater. Sci. Eng.* **2019**, *589*, 1–9. [CrossRef]
7. Hull, A.; O'Holleran, C. Bicycle infrastructure: can good design encourage cycling? *Urban, Plan. Transp. Res.* **2014**, *2*, 369–406. [CrossRef]
8. Shin, S. Trend of Process Automation and Factory Automation. In Proceedings of the 2006 SICE-ICASE International Joint Conference, Busan, Korea, 18–21 October 2006.
9. Merdan, M.; Lepuschitz, W.; Axinia, E. Advanced process automation using automation agents. In Proceedings of the 5th International Conference on Automation, Robotics and Applications, Wellington, New Zealand, 6–8 December 2011.
10. Zhou, C.; Huang, S.; Xiong, N.; Yang, S.H.; Li, H.; Qin, Y.; Li, X. Design and Analysis of Multimodel-Based Anomaly Intrusion Detection Systems in Industrial Process Automation. *IEEE Trans. Systs. Man. Cybern. Systs.* **2015**, *45*, 1345–1360. [CrossRef]
11. Jiao, Z.J.; He, C.Y.; Wang, J.; Zhao, Z. Development and application of automation control system to plate production line. In Proceedings of the 2010 11th International Conference on Control Automation Robotics & Vision, Singapore, 7–10 December 2010.
12. Lin, H.C.; Li, L.L.; Lee, V.C.S. Multiple Autonomous Robots Coordination and Navigation. *J. Robot.* **2019**, *2019*, 1–2. [CrossRef]
13. Ito, S.; Kikuchi, H.; Chen, Y.; Shimizu, Y.; Gao, W.; Takahashi, K.; Kanayama, T.; Arakawa, K.; Hayashi, A. A Micro-Coordinate Measurement Machine (CMM) for Large-Scale Dimensional Measurement of Micro-Slits. *Appl. Sci.* **2016**, *6*, 156. [CrossRef]
14. Pawar, M.G.; Nandeshwar, B.S.; Borikar, V.N.; Jaiswal, S.B. Design of Portable Coordinate Measuring Machine. *Int. J. Emerg. Eng. Res. Technol.* **2015**, *3*, 1–9.
15. Puertas, C.; Luis Pérez, J.; Salcedo, D.; León, J.; Luri, R.; Fuertes, J.P. Precision Study of a Coordinate Measuring Machine Using Several Contact Probes. *Procedia. Eng.* **2013**, *63*, 547–555. [CrossRef]
16. Anagnostakis, D.; Ritchie, J.; Lim, T.; Sung, R.; Dewar, R. Automated Coordinate Measuring Machine Inspection Planning Knowledge Capture and Formalization. *J. Comput. Inf. Sci. Eng.* **2018**, *18*, 1–12. [CrossRef]
17. Mian, S.H.; Al-Ahmari, A. New developments in coordinate measuring machines for manufacturing industries. *Int. J. Metrol. Qual. Eng.* **2014**, *5*, 1–10.
18. Majeed, A.; Lee, S. A Fast Global Flight Path Planning Algorithm Based on Space Circumscription and Sparse Visibility Graph for Unmanned Aerial Vehicle. *Electron* **2018**, *7*, 375. [CrossRef]
19. Plaku, E.; Plaku, E.; Simari, P. Direct Path Superfacets: An Intermediate Representation for Motion Planning. *IEEE Robot. Autom. Lett.* **2016**, *2*, 350–357. [CrossRef]
20. Jahnavi, K.; Sivraj, P. Teaching and learning robotic arm model. In Proceedings of the 2017 International Conference on Intelligent Computing, Instrumentation and Control Technologies (ICICICT), Kannur, India, 6–7 July 2017.

21. Elhoseny, M.; Shehab, A.; Yuan, X. Optimizing robot path in dynamic environments using Genetic Algorithm and Bezier Curve. *J. Intell. Fuzzy. Syst.* **2017**, *33*, 2305–2316. [CrossRef]
22. Juan, B.V.; David, M.V.; Luis, C.L.; Luis, M.G. A low-cost platform based on a robotic arm for parameters estimation of Inertial Measurement Units. *Measurement* **2017**, *110*, 257–262.